doi:10.1038/nature17141

1. Materials synthesis and characterization

The dithienylcyclopentene based axially chiral molecular switch (*S*,*S*)-**D4** was synthesized according to the route given in Scheme 1. For comparison, a similar chiral molecular switch (*S*,*S*)-**D1** and an azobenzene based chiral switch **Azo** are also synthesized. The synthesis routes of (*S*,*S*)-**D1** and **Azo** are shown in Scheme 1 and Scheme 2, respectively. The synthetic methods were the same as those reported in our previously published paper[1-3]. The chemical structures were identified by ^{1}H NMR (400 MHz) and ^{13}C NMR (50 MHz) spectra respectively. The coupling constants (*J*) were reported in hertz (Hz), while the splitting pattern was designated as s, singlet; d, doublet; t, triplet; and m, multiplet. High resolution mass spectrometry was used for analysis.

Synthesis and characterizations of light-driven chiral switches (*S*,*S*)-**D4** ***and*** (*S*,*S*)-**D1**

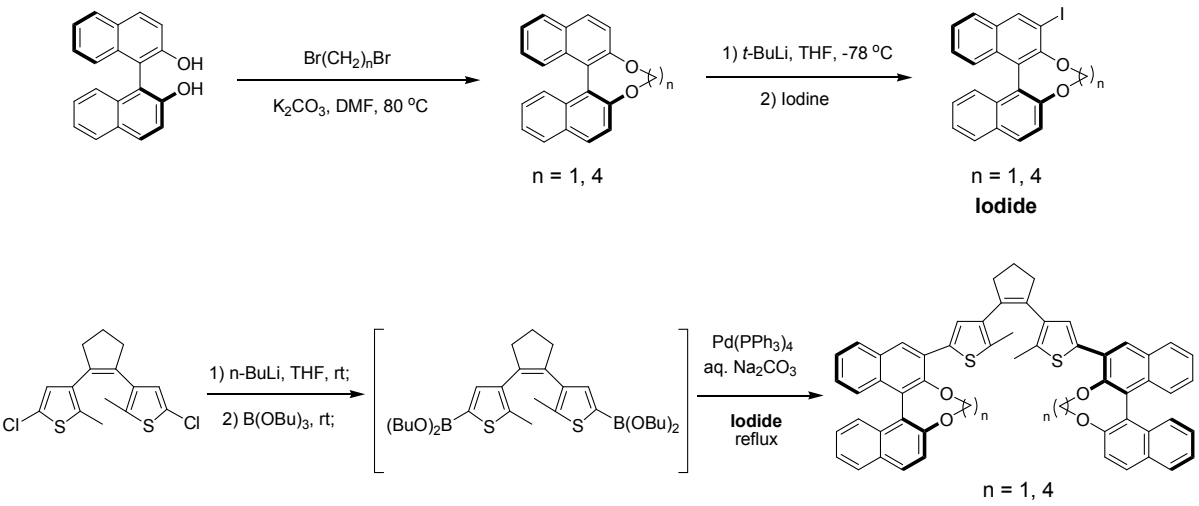

Scheme 1 | Synthesis routes for chiral switches (*S*,*S*)-D4 (n=4) and (*S*,*S*)-D1 (n=1)[1,2].

Chemical characterization data of intermediates and (*S*,*S*)-**D4**:

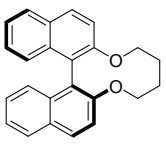

^{1}H NMR (400 MHz, $CDCl_3$): δ = 7.95 (d, *J* = 8.4 Hz, 2H), 7.87 (d, *J* = 8.0 Hz, 2H), 7.50 (d, *J* = 8.8 Hz, 2H),

7.34 (t, J = 8.0 Hz, 2H), 7.19 (t, J = 8.0 Hz, 2H), 7.10 (d, J = 8.4 Hz), 4.55-4.51 (m, 2H), 4.15-4.10 (m, 2H), 1.89-1.83 (m, 2H), 1.76-1.72 (m, 2H). ^{13}C NMR (50 MHz, $CDCl_3$): δ = 153.3, 134.1, 129.8, 129.3, 127.9, 126.3, 125.8, 124.0, 122.4, 117.4, 70.3, 25.3. HRMS (ESI) Calcd for $C_{24}H_{20}O_2Na^+$: 363.1361; found: 363.1377.

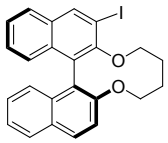

^{1}H NMR (400 MHz, $CDCl_3$): δ = 8.52 (s, 1H), 7.96 (d, J = 9.2 Hz, 1H), 7.84 (d, J = 8.4 Hz, 1H), 7.75 (d, J = 8.4 Hz, 1H), 7.49 (d, J = 9.2 Hz, 1H), 7.37-7.29 (m, 2H), 7.21-7.12 (m, 2H), 7.01 (d, J = 8.4 Hz, 1H), 6.75 (d, J = 8.0 Hz, 1H), 4.79-4.72 (m, 2H), 4.25 (td, J = 10.4, 2.0 Hz, 1H), 4.08 (t, J = 12.0 Hz, 1H), 2.03-1.84 (m, 2H), 1.72-1.53 (m, 2H). ^{13}C NMR (50 MHz, $CDCl_3$): δ = 153.2, 152.3, 140.3, 134.3, 134.2, 132.0, 129.8, 127.8, 126.9, 126.64, 126.56, 126.3, 125.44, 125.36, 124.2, 122.1, 117.4, 89.0, 72.2, 69.7, 26.5, 23.4. HRMS (ESI) Calcd for $C_{24}H_{19}IO_2Na^+$: 489.0328; found: 489.0321.

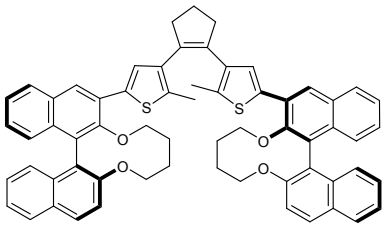

^{1}H NMR (400 MHz, $CDCl_3$): δ = 7.96-7.94 (m, 4H), 7.83 (t, J = 8.8 Hz, 4H), 7.48 (d, J = 9.2 Hz, 2H), 7.36-7.29 (m, 4H), 7.19-7.14 (m, 6H), 7.02-6.96 (m, 4H), 4.63-4.60 (m, 2H), 3.95-3.80 (m, 6H), 2.89-2.78 (m, 4H), 2.17 (s, 6H), 2.10-2.03 (m, 2H), 1.88-1.79 (m, 2H), 1.58-1.51 (m, 2H), 1.40-1.28 (m, 4H). ^{13}C NMR (50 MHz, $CDCl_3$): δ = 152.3, 151.9, 136.6, 136.5, 135.0, 134.9, 134.4, 133.6, 130.4, 129.9, 129.8, 129.4, 128.1, 127.8, 126.44, 126.37, 126.0, 125.7, 125.6, 124.9, 124.1, 122.7, 117.4, 71.3, 69.4, 38.3, 26.3, 23.3, 14.4. HRMS (ESI) Calcd for $C_{63}H_{52}O_4S_2Na^+$: 959.3205; found: 959.3182.

Chemical characterization data of intermediates and (*S*,*S*)-**D1**:

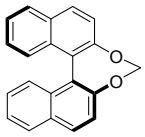

^{1}H NMR ($CDCl_3$, 200 MHz): δ = 8.01-7.92 (m, 4H), 7.54-7.41 (m, 6H), 7.35-7.30 (m, 2H), 5.70 (s, 2H). ^{13}C NMR ($CDCl_3$, 50 MHz): δ = 151.2, 132.2, 131.8, 130.3, 128.4, 126.9, 126.08, 126.05, 125.0, 120.9, 103.1. HRMS (ESI) Calcd for $C_{21}H_{14}O_2Na^+$: 321.0891, found: 321.0898.

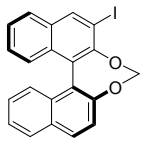

^{1}H NMR ($CDCl_3$, 400 MHz): δ = 8.50 (s, 1H), 8.00 (d, J = 9.2 Hz, 1H), 7.94 (dd, J = 8.8, 1.2 Hz, 1H), 7.83 (d, J = 8.4 Hz, 1H), 7.50-7.43 (m, 5H), 7.33-7.28 (m, 2H), 5.71 (d, J = 3.6 Hz, 1H), 5.67 (d, J = 3.6 Hz, 1H). ^{13}C NMR ($CDCl_3$, 50 MHz): δ = 151.5, 149.3, 139.2, 133.1, 132.0, 131.7, 130.7, 128.4, 127.3, 127.0, 126.9, 126.7, 126.5, 126.2, 125.8, 125.1, 120.8, 102.6, 90.2. Anal Calcd for $C_{21}H_{13}IO_2$: C, 59.45, H, 3.09; found: C, 59.22, H, 2.94. HRMS (ESI) Calcd for $C_{21}H_{13}IO_2Na^+$: 446.9858, found: 446.9840.

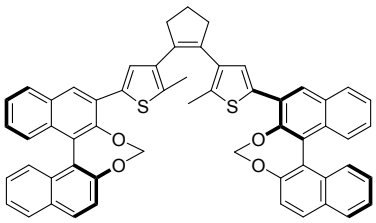

^{1}H NMR ($CDCl_3$, 400 MHz): δ = 8.16 (s, 2H), 7.94 (d, J = 8.8 Hz, 2H), 7.93 (d, J = 8.0 Hz, 2H), 7.50 (d, J = 8.8 Hz, 2H), 7.47-7.43 (m, 2H), 7.41-7.35 (m, 8H), 7.32-7.28 (m, 2H), 7.24-7.20 (m, 2H), 5.59 (d, J = 3.6 Hz, 2H), 5.56 (d, J = 3.2 Hz, 2H), 2.92-2.90 (m, 4H), 2.15-2.11 (m, 2H), 2.13 (s, 6H). ^{13}C NMR ($CDCl_3$, 50 MHz): δ = 151.2, 147.6, 136.3, 136.0, 134.9, 134.1, 132.2, 131.7, 131.6, 131.1, 130.3, 128.4, 127.8, 127.4, 127.2, 126.9, 126.7, 126.2, 126.1, 125.8, 125.5, 125.0, 120.8, 102.4, 38.4, 23.1, 14.3. Anal Calcd for $C_{57}H_{40}O_4S_2$: C, 80.25, H, 4.73; found: C, 80.27, H, 5.01. HRMS (ESI) Calcd for $C_{57}H_{40}O_4S_2Na^+$: 875.2266, found: 875.2241.

***Synthesis and characterization of chiral switch* Azo**

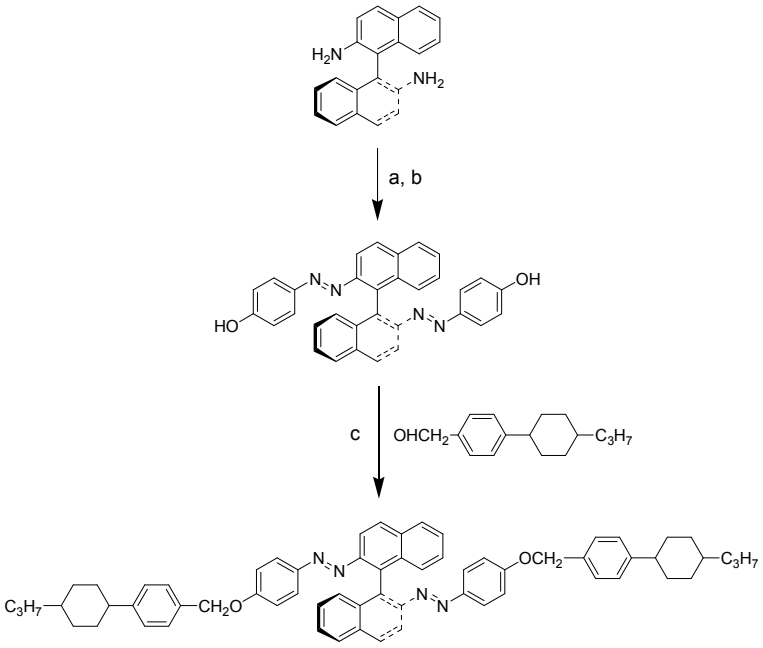

Scheme 2 | Synthesis route for chiral switch Azo[3].

Chemical characterization data of intermediates and chiral switch **Azo**:

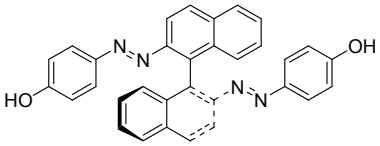

^{1}H NMR (200 MHz, Acetone): δ = 8.96 (s, 2H), 8.07-8.18 (m, 2H), 7.55 (m, 2H), 7.31-7.38 (m, 8H), 6.73 (d, J = 6.8 Hz, 4H). ^{13}C NMR (50 MHz, Acetone): δ = 160.98, 148.98, 147.26, 137.11, 134.94, 134.88, 129.64, 128.88, 127.91, 127.68, 127.33, 125.25, 116.17, 114.97.

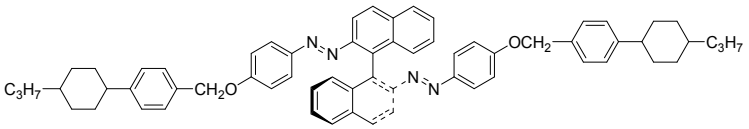

^{1}H NMR (200 MHz, $CDCl_3$): δ = 7.95 (d, J = 8.8 Hz, 2H), 7.73-7.85 (m, 4H), 7.21-7.30 (m, 4H), 6.95-7.12 (m, 14H), 6.57 (d, J = 8.8 Hz, 4H), 4.73 (s, 4H), 2.24 (t, J = 12.0 Hz, 2H), 1.64 (d, J = 10.6 Hz, 8H), 0.74-1.47 (m, 18H), 0.69 (t, J = 7.0 Hz, 6H). ^{13}C NMR (50 MHz, $CDCl_3$): δ = 160.88, 148.30, 147.91,

147.35, 136.69, 134.25, 134.19, 133.73, 128.96, 128.02, 127.79, 127.59, 127.07, 126.91, 126.54, 124.57, 114.73, 114.45, 70.05, 44.35, 39.68, 36.97, 34.27, 33.51, 20.01, 14.40. Anal Calcd for $C_{64}H_{66}N_4O_2$: C, 83.26; H, 7.21; N, 6.07. Found: C, 83.33; H, 7.37; N, 6.19.

HRMS (ESI) Calcd for $C_{64}H_{66}N_4O_2H^+$: 923.5264, found: 923.5280.

2. Handedness analysis of the standing helix (SH)

Due to the long helical pitch of the cholesteric liquid crystal (CLC) which far exceeds the wavelength of visible light, it is difficult to identify the handedness through common methods. To confirm handedness, an optical setup shown in Figure 1 was established. The sample was placed horizontally on the objective stage of a polarizing optical microscope (POM). The rubbing direction (***R***) was parallel to the x-axis. Incoming light with polarization along the x-axis successively passed through the LC cell, a quarter waveplate (fast axis: x-axis), a second quarter waveplate (fast axis: 45° with x-axis), and an analyzer (***A***: x-axis). The transmission was analyzed with the Jones Matrix methodology and images were captured by a CCD camera.

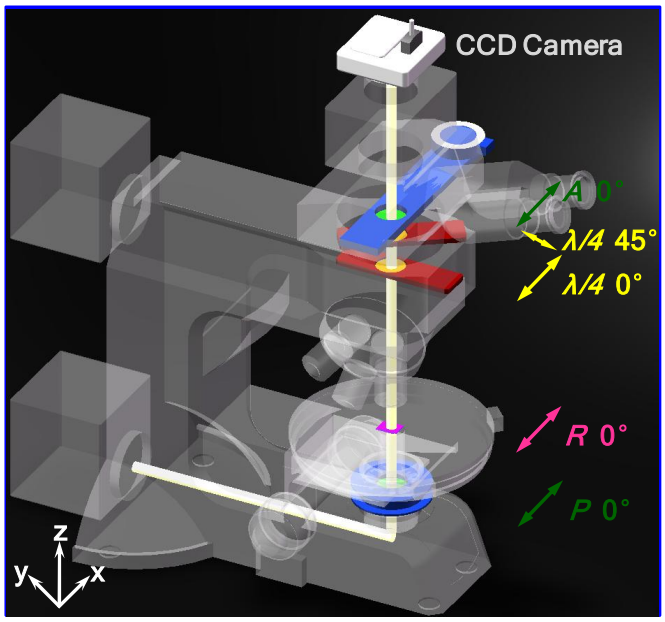

Figure 1 | Microscope arrangement used for confirming the handedness of SH arrangement. The optical axis and rubbing direction angles relative to the x-axis are labeled.

For a twisted aligned LC with a SH state, if the twist angle is $\varphi_0 > 0$, the Jones Matrix can be expressed as[4]:

$$M_{\varphi_0} = \begin{pmatrix} a & b \\ c & d \end{pmatrix} \tag{S1}$$

in which,

$$a = \cos\varphi_0 \cos\beta + \frac{1}{\sqrt{1+\alpha^2}} \sin\varphi_0 \sin\beta + i\frac{\alpha}{\sqrt{1+\alpha^2}} \cos\varphi_0 \sin\beta \tag{S2}$$

$$b = -\sin\varphi_0 \cos\beta + \frac{1}{\sqrt{1+\alpha^2}} \cos\varphi_0 \sin\beta + i\frac{\alpha}{\sqrt{1+\alpha^2}} \sin\varphi_0 \sin\beta \tag{S3}$$

$$c = \sin\varphi_0 \cos\beta - \frac{1}{\sqrt{1+\alpha^2}} \cos\varphi_0 \sin\beta + i\frac{\alpha}{\sqrt{1+\alpha^2}} \sin\varphi_0 \sin\beta \tag{S4}$$

$$d = \cos\varphi_0 \cos\beta + \frac{1}{\sqrt{1+\alpha^2}} \sin\varphi_0 \sin\beta - i\frac{\alpha}{\sqrt{1+\alpha^2}} \cos\varphi_0 \sin\beta \tag{S5}$$

In Eqs. (S2)~(S5),

$$\alpha = \frac{\Delta n d}{\lambda \varphi_0} \pi \tag{S6}$$

$$\beta = \varphi_0 \sqrt{1+\alpha^2} \tag{S7}$$

If the twist angle in a right-handed-SH (RH-SH) is φ_0, the twist angle in a left-handed-SH (LH-SH) is $-\varphi_0$, and the Jones Matrix of a LH-SH state becomes,

$$M_{-\varphi_0} = \begin{pmatrix} A & B \\ C & D \end{pmatrix} \tag{S8}$$

where $A = a$, $B = -b$, $C = -c$, $D = d$.

The transmission matrixes for the cases where the LC arrangements (states) are RH-SH and LH-SH are respectively expressed as,

$$\Omega_{\varphi_0} = \begin{pmatrix} 1 & 0 \\ 0 & 0 \end{pmatrix} \bullet \frac{1}{\sqrt{2}} \begin{pmatrix} 1 & i \\ i & 1 \end{pmatrix} \bullet \begin{pmatrix} 1 & 0 \\ 0 & i \end{pmatrix} \bullet \begin{pmatrix} a & b \\ c & d \end{pmatrix} \bullet \begin{pmatrix} 1 \\ 0 \end{pmatrix}$$

$$= \frac{1}{\sqrt{2}} M \bullet e^{i\psi_1} \begin{pmatrix} 1 + N \bullet e^{i(\frac{\pi}{2} + \psi_2 - \psi_1)} \\ 0 \end{pmatrix} \tag{S9}$$

$$\Omega_{-\varphi_0} = \begin{pmatrix} 1 & 0 \\ 0 & 0 \end{pmatrix} \bullet \frac{1}{\sqrt{2}} \begin{pmatrix} 1 & i \\ i & 1 \end{pmatrix} \bullet \begin{pmatrix} 1 & 0 \\ 0 & i \end{pmatrix} \bullet \begin{pmatrix} A & B \\ C & D \end{pmatrix} \bullet \begin{pmatrix} 1 \\ 0 \end{pmatrix}$$

$$= \frac{1}{\sqrt{2}} M \bullet e^{i\psi_1} \begin{pmatrix} 1 - N \bullet e^{i(\frac{\pi}{2} + \psi_2 - \psi_1)} \\ 0 \end{pmatrix} \tag{S10}$$

in which,

$$M = \sqrt{X_1^2 + Y_1^2}\ ; N = \sqrt{\frac{X_2^2 + Y_2^2}{X_1^2 + Y_1^2}};\ \psi_1 = \tan^{-1}\left(\frac{Y_1}{X_1}\right);\ \psi_2 = \tan^{-1}\left(\frac{Y_2}{X_2}\right) \tag{S11}$$

$$X_1 = \cos\varphi_0 \cos\beta + \frac{1}{\sqrt{1+\alpha^2}} \sin\varphi_0 \sin\beta \tag{S12}$$

$$Y_1 = \frac{\alpha}{\sqrt{1+\alpha^2}} \cos\varphi_0 \sin\beta \tag{S13}$$

$$X_2 = -\frac{\alpha}{\sqrt{1+\alpha^2}} \sin\varphi_0 \sin\beta \tag{S14}$$

$$Y_2 = \sin\varphi_0 \cos\beta - \frac{1}{\sqrt{1+\alpha^2}} \cos\varphi_0 \sin\beta \tag{S15}$$

According to Eqs. (S9) and (S10), the transmission intensities for the RH-SH and LH-SH states can be deduced respectively as,

$$I_{\varphi_0} = \Omega_{\varphi_0} \bullet \Omega_{\varphi_0}^*$$

$$= \frac{M^2}{2}\left[N^2 + 1 + 2N\cos(\frac{\pi}{2} + \psi_2 - \psi_1)\right] \tag{S16}$$

$$I_{-\varphi_0} = \Omega_{-\varphi_0} \bullet \Omega_{-\varphi_0}^*$$

$$= \frac{M^2}{2}\left[N^2 + 1 - 2N\cos(\frac{\pi}{2} + \psi_2 - \psi_1)\right] \tag{S17}$$

Combining these with Eqs. (S11)-(S15) and considering the experimental conditions (Δn=0.159; d=3.7 μm), we obtain that $2N\cos(\frac{\pi}{2} + \psi_2 - \psi_1) > 0$, therefore,

$$I_{\varphi_0} > I_{-\varphi_0} \tag{S18}$$

which implies that the transmission intensity for a RH-SH state will be higher than that of a LH-SH state.

Figure 2 shows the texture of the RH-SH and LH-SH state, respectively, and clearly indicates the brightness is higher in the RH-SH state.

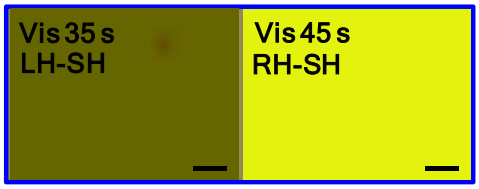

Figure 2 | Textures captured using the optical setup shown in Figure 1. The LH-SH and RH-SH states correspond to those shown in the Main Text Figure 1d. Scale bar: 10 μm.

3. UV-induced three-dimensional control over the helical axis

The uniform left-handed LH (Figure 3l) can be recovered from the uniform right-handed LH (Figure 3a) by UV irradiation, passing through the right-handed SH (Figure 3e), the unwound homogeneous alignment (Figure 3f), the re-generated SH arrangement with left-handedness (Figure 3g), finally reaching the left-handed uniform LH (Figure 3i-l).

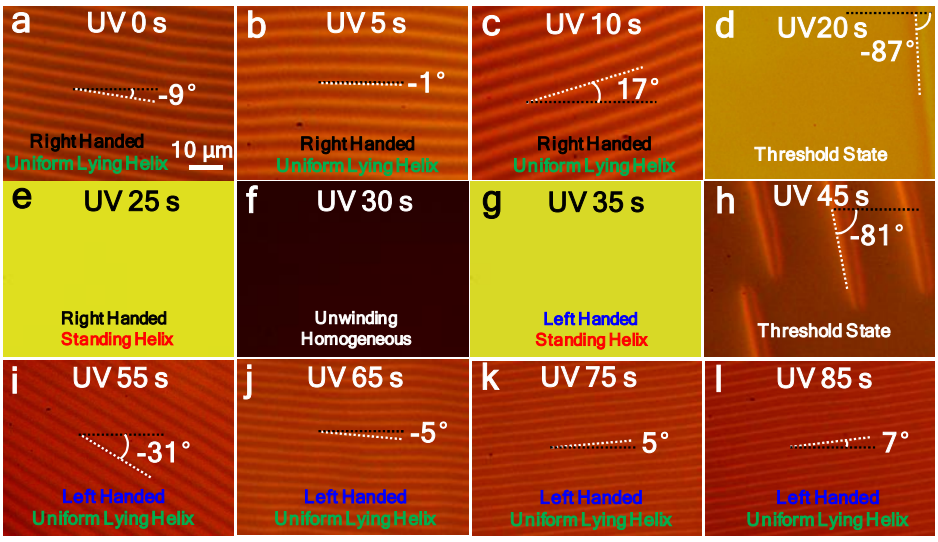

Figure 3 | Recovery of the helical superstructure by irradiation of UV light. Concentration of chiral switch (*S*,*S*)-**D4** is 1.2 mol%. Rubbing direction is along the horizontal direction (black dashed line).

4. Analysis of the lying helix (LH) formation

One key aspect for the formation of a uniform LH is generating either a large oblique angle or vertical alignment of LCs. The sample in the original state and at the threshold state were observed with conoscopy. A pink bright state was observed initially which gradually transformed to a blurry dark brush at the threshold state indicative of a large oblique angle of LCs relative to the substrate (insets at the right corner of Figure 4). Molecular dynamics (MD) simulations from an initial planar homogeneous alignment confirms this behavior. Upon light stimulation, the molecules stand up generating a large oblique angle of the director relative to the substrate (Figure 4b). The coordinates of the LC director corresponding to the two cases, denoted by an azimuthal and polar angle (φ, θ), are given at the left corners of the figures. The large oblique direction of the LCs coupled with the strong free energy of system overcomes the standing helix configuration, leading to the lying down of the helix. The uniform direction of these lying helixes is maintained due to the anti-parallel alignment treatment on the substrates. The above experimental observations and simulation results describe well the formation and uniform orientation of the stripes in the CLC phase. The twisted helical structure is not observed in the models shown in Figure 4 due to the small dimension along the helical axis (z-axis), 4 nm.

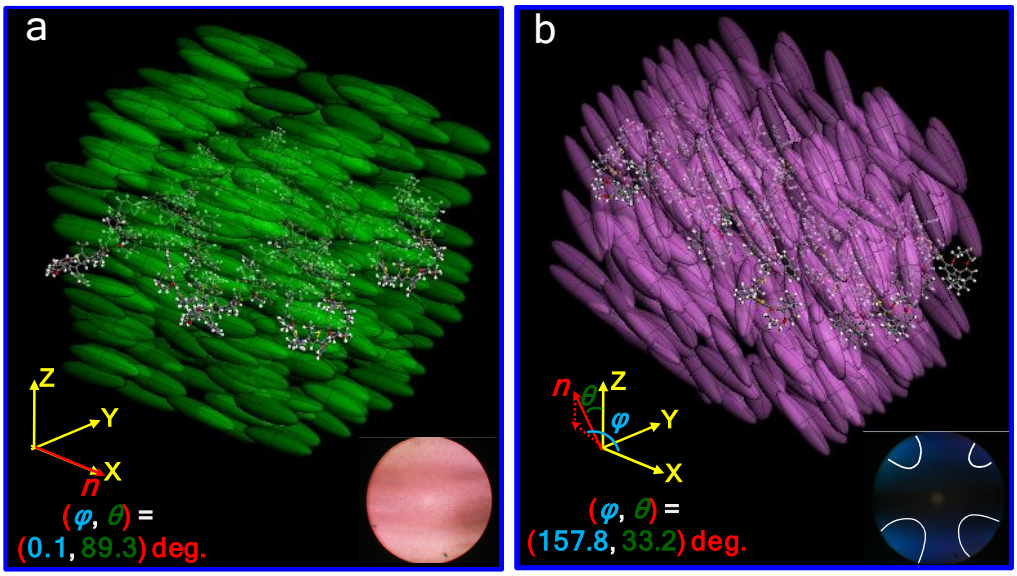

Figure 4 | LCs arrangements at the initial (a) and the threshold state (b). The chiral switch molecules

were inserted in the center of the LC layer. Textures under conoscopy and the coordinates of LC director are shown at the right corner and left corner, respectively.

5. Comparison of textures for the samples containing different chiral switches

For comparison, three samples, one containing the chiral switch with handedness inversion (*S*,*S*)-**D4** and two without handedness inversion (*S*,*S*)-**D1** and **Azo** were irradiated. Textures at the PSS_{vis} (photostationary state induced by visible-light irradiation) and PSS_{UV} (photostationary state induced by UV-light irradiation) states in 3.7-μm and 5.1-μm thick cells are shown in Figure 5 for all three switches. A non-uniform arrangement of stripes forms in the sample containing (*S*,*S*)-**D1** in the 5.1-μm cell (Figure 5k and l). The uniform LH arrangement forms in the same sample when it was confined to the thinner 3.7-μm cell (Figure 5e and f). Non-uniformity increases in thicker cells due to the reduced influence of the anchoring conditions. The distribution of the LC director in the middle layer is more easily disturbed by the deformation of chiral switch molecules during light irradiation. The uniform LH forms in the samples containing the chiral switch whether it exhibits handedness inversion or not, if the surface anchoring is strong enough (Figure 5a~f).

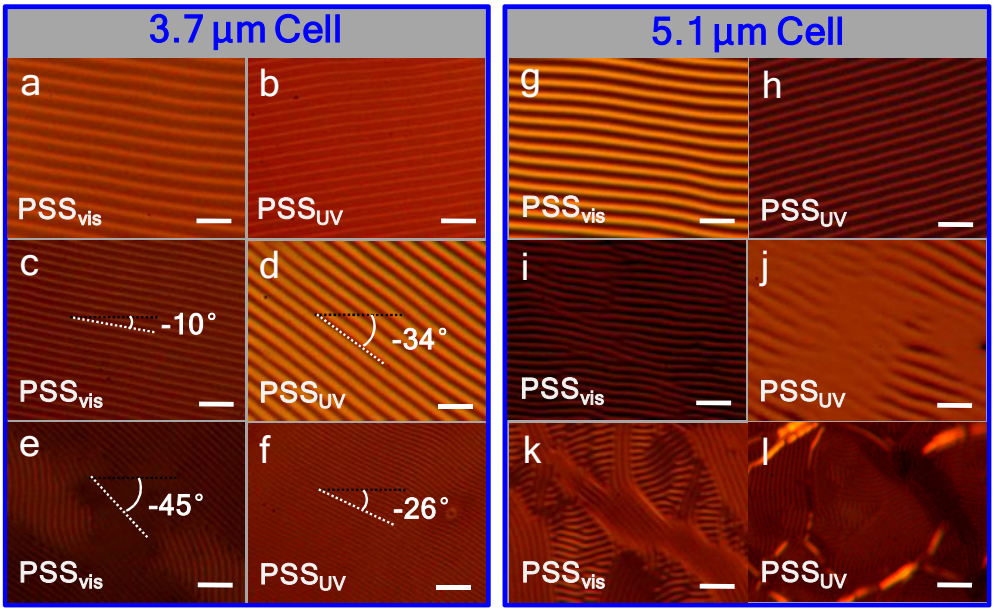

Figure 5 | Textures of samples containing chiral switches with handedness inversion (*S*,*S*)-D4 (1.2 mol%. a, b, g, h) and without handedness inversion Azo (0.5 mol%. c, d, i, j), (*S*,*S*)-D1 (0.43 mol%. e, f, k, l) after irradiation

by light. The directions of stripes in c, d, e and f planes were labeled with a white dashed line, and the angles with respect to the horizontal are given. The rotation angle for the samples containing **Azo** and (*S*,*S*)-**D1** are 24° and 19°, respectively. Scale bar: 10 μm.

6. Cell gap-to-pitch ratio at the threshold state - $[d/P]_{th}$

Many previous reports indicate that the cell gap (***d***)-to-pitch (***P***) ratio is of key importance for the formation of a LH texture in CLCs[5-7]. The value of $[d/P]_{th}$ for samples containing (*S*,*S*)-**D4** is very close to integer multiples of 0.5 as shown in Figure 6a. This was true for both thickness cells studied in Figure 5. The value of $[d/P]_{th}$ of different samples confined in different cell gaps are shown in Figure 6a and the corresponding HTPs are given in Figure 6b.

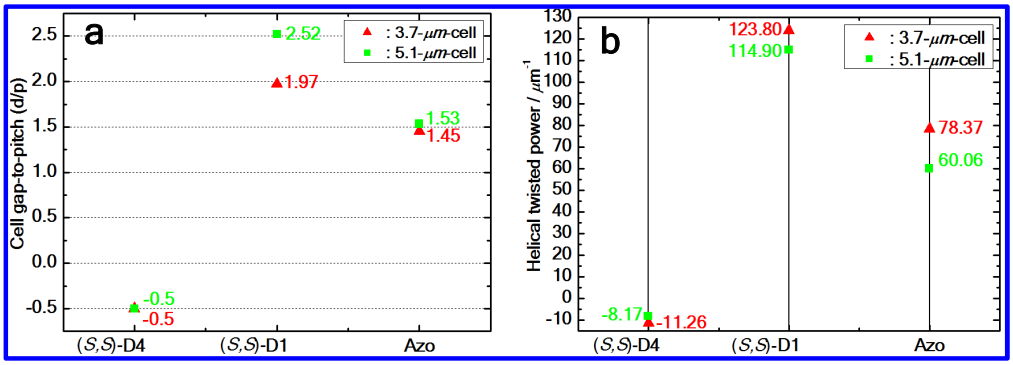

Figure 6 | The value of $[d/P]_{th}$ for samples with different chiral switches confined in different cell gaps (a) and the corresponding HTPs (b). The negative values are caused by handedness inversion of the helical superstructure. The compositions of the samples are the same as those shown in Figure 5.

7. Optimized geometry of chiral switches

The perturbation caused by the deformation of the chiral switches can be analyzed from the viewpoint of molecular structure. Figure 7 exhibits the optimized geometric atomistic models of the three switches studied, (*S*,*S*)-**D4**, (*S*,*S*)-**D1** and **Azo** before and after light irradiation. The dithienylcyclopentene derivatives (*S*,*S*)-**D4** and (*S*,*S*)-**D1** have a very similar chemical structure. During photocyclization, one of the

five-membered ring, α, rotates out of plane towards the observer and other one, β, goes behind the plane away from the observer due to the two carbon-carbon bonds connecting the central five-membered ring. This yields the rotation of two binaphthyl groups, A and B, around the axes of *C1-C2* and *C3-C4* respectively in opposite directions. This causes the changes in the direction of the two chiral axes, *C5-C6* and *C7-C8*. Upon comparison of (*S*,*S*)-**D1** with (*S*,*S*)-**D4**, the most significant difference is that the two chiral axes in (*S*,*S*)-**D4** generate a dramatic direction change, while little change in (*S*,*S*)-**D1** is evident after photocyclization. In addition, the rotations of the two binaphthyl groups, connected at the two sides of the molecules, are larger in (*S*,*S*)-**D4**, yielding a stronger perturbation to the LC arrangement. The molecular deformation for **Azo**, a transformation from the scissor-like *trans*-isomer to the 'w'-shaped *cis*-isomer, leads to a remarkable change of the HTP, yet there is almost no change in the direction of the chiral axis.

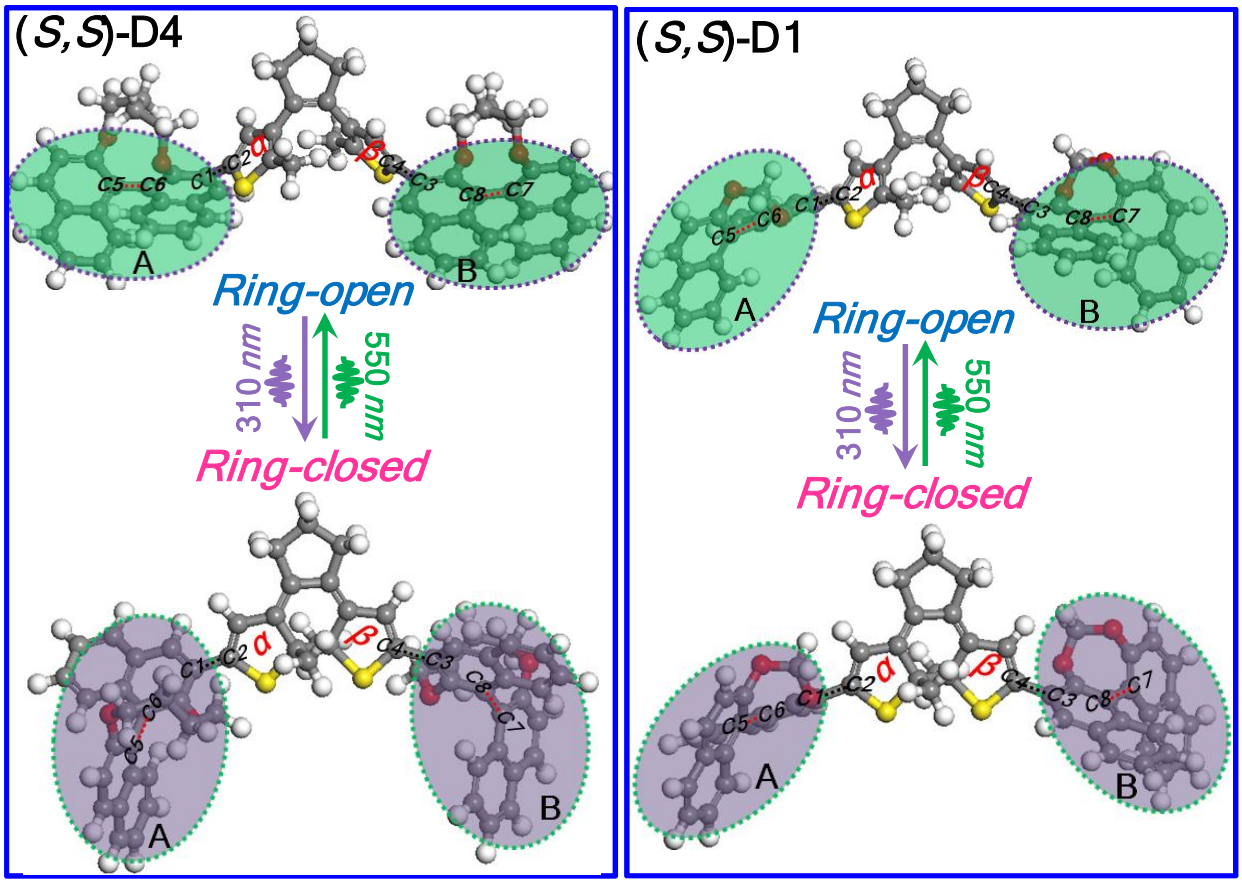

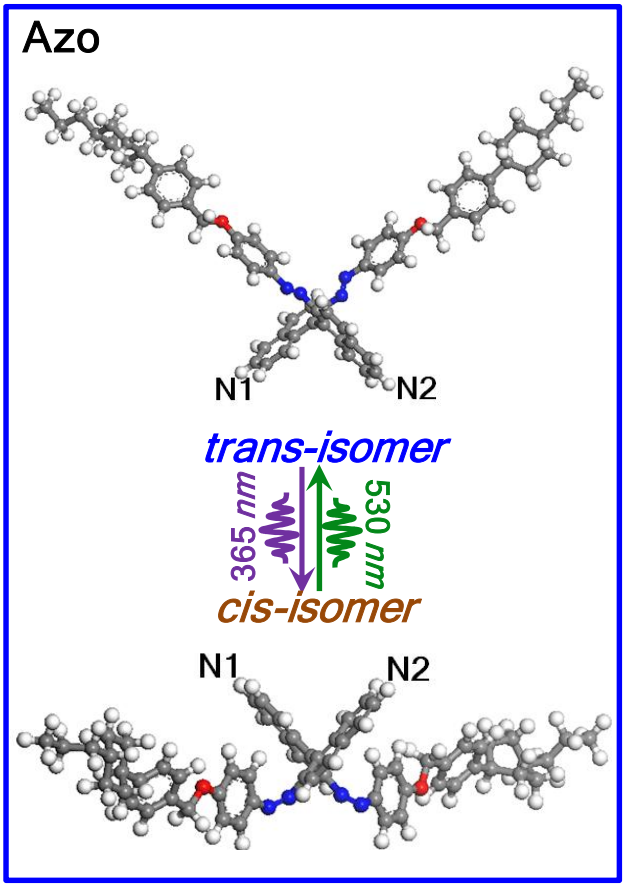

Figure 7 | Optimized geometrical atomistic models of the two isomers for (*S*,*S*)-D4, (*S*,*S*)-D1 and Azo.

8. Influence of thicker cells on the formation of the uniform LH

The overall influence of surface anchoring diminishes as the cell thickness increases[8]. The same samples were injected into 8-μm-thick cells and irradiated with the UV light. No uniform LH formed (Figure 8) even in samples where the concentration of **Azo** was increased to either 1.7 mol% or 3.4 mol% (Figure 9).

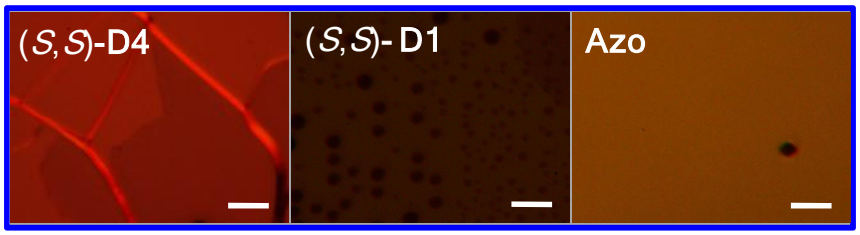

Figure 8 | Textures of the samples containing (*S*,*S*)-D4, (*S*,*S*)-D1 and Azo after irradiated by UV light with intensity of 2.2 mW/cm^2. Cell gap: 8 μm; scale bar: 10 μm.

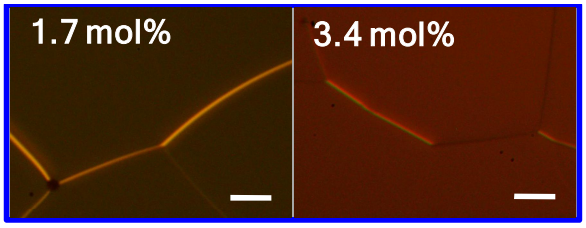

Figure 9 | Textures for the samples containing 1.7 mol% and 3.4 mol% of Azo after irradiation by UV light with intensity of 2.2 mW/cm^2. Cell gap: 8 μm; scale bar: 10 μm.

9. In-plane stripe rotation for the sample containing (*S*,*S*)-D4 (1.2 mol%) upon UV-irradiation

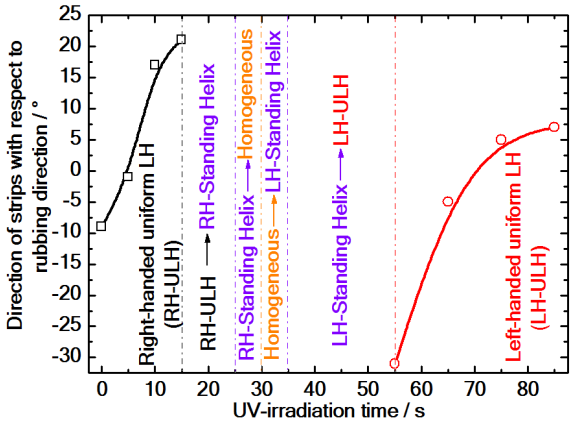

Figure 10 | Sample at PSS_{vis} state was irradiated by the UV light. The right-handed uniform lying helix rotated from -9°~21° (black curve connecting black squares), while the left-handed uniform lying helix rotated from -31°~7°(red curve connecting red circles). The helical axis can therefore be manipulated over the range from -31°~21° by light.

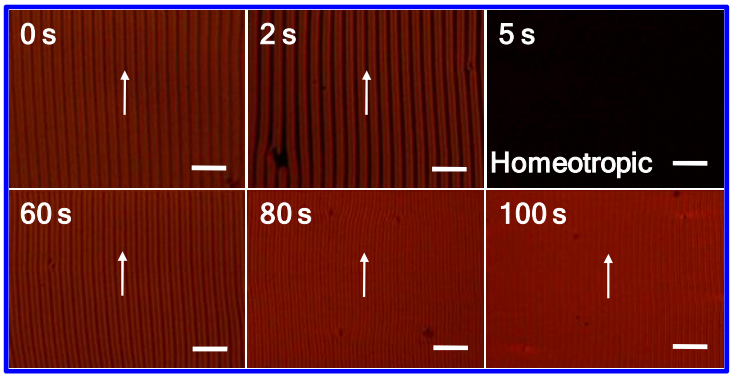

Figure 11 | Uniform LH texture during UV irradiation with a strong anchoring (1.0-V voltage was applied) to the molecules. The white arrow denotes the direction of stripes. Sample containing (*S*,*S*)-**D4** (1.2 mol%) confined in 3.7-μm-thick cell. Scale bar: 10 μm.

10. Comparison of thermo-relaxation between samples containing dithienylcyclopentene derivative (*S*,*S*)-D4 and the azobenzene based Azo

One advantage of the chiral switch (*S*,*S*)-**D4** is its excellent thermal stability. Figure 12 shows the diffraction properties based on the uniform LH arrangement for the sample containing (*S*,*S*)-**D4** (1.2 mol%). The uniform LH structure is very stable at PSS_{vis} (Figure 12a), PSS_{UV} (Figure 12d), and at any intermediate state (Figure 12b and c). Although the relaxation performance over 12 hours is shown, experiments indicate it is maintained ≥3 days. As a comparison, the sample containing the **Azo** (0.5 mol%) switch (Figure 13) relaxed back to the original state within 8 minutes.

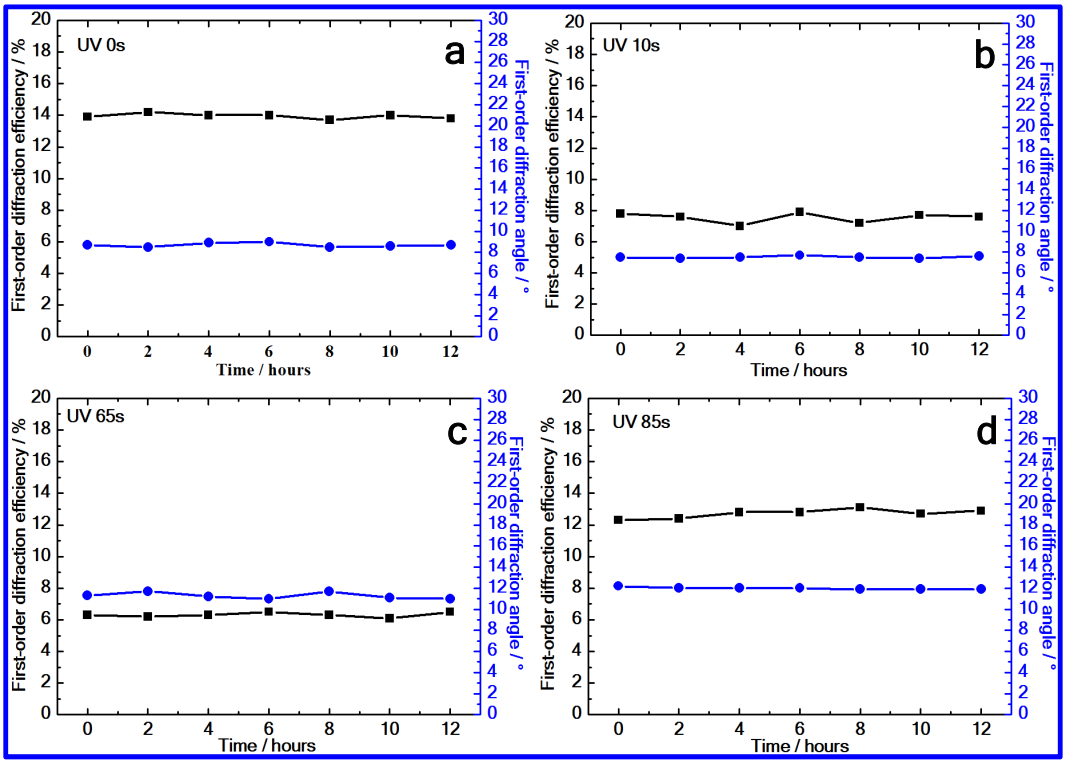

Figure 12 | Changes of the first-order diffraction efficiency and first-order diffraction angle for the uniform LH at PSS_{vis} (a), PSS_{UV} (d) and two intermediate states (b and c), within 12 hours.

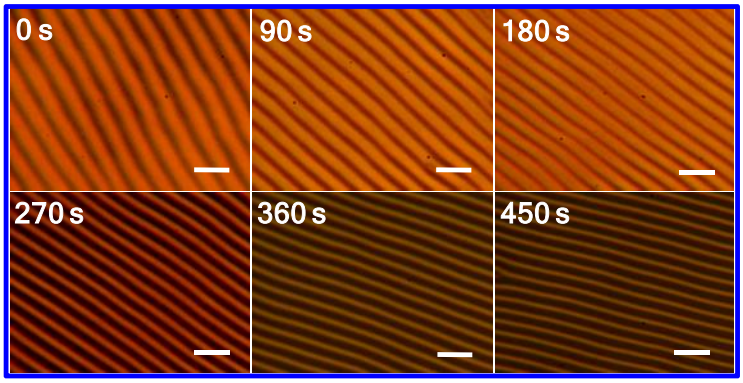

Figure 13 | Texture of uniform LH changes after the UV-stimulus was removed. The chiral switch is **Azo** with the concentration of 0.5 mol%. The cell gap is 3.7 μm.

11. Oscillation of two-dimensional beam steering from the intermediate state

The two-dimensional beam steering can be driven back-and-forth from an intermediate state (UV-irradiation for 15 s, as shown in Figure 14 'UV 15s') by the alternating use of UV- and visible-light irradiation (Figure 14) demonstrating reversible (back-and-forth) 2D beam scanning.

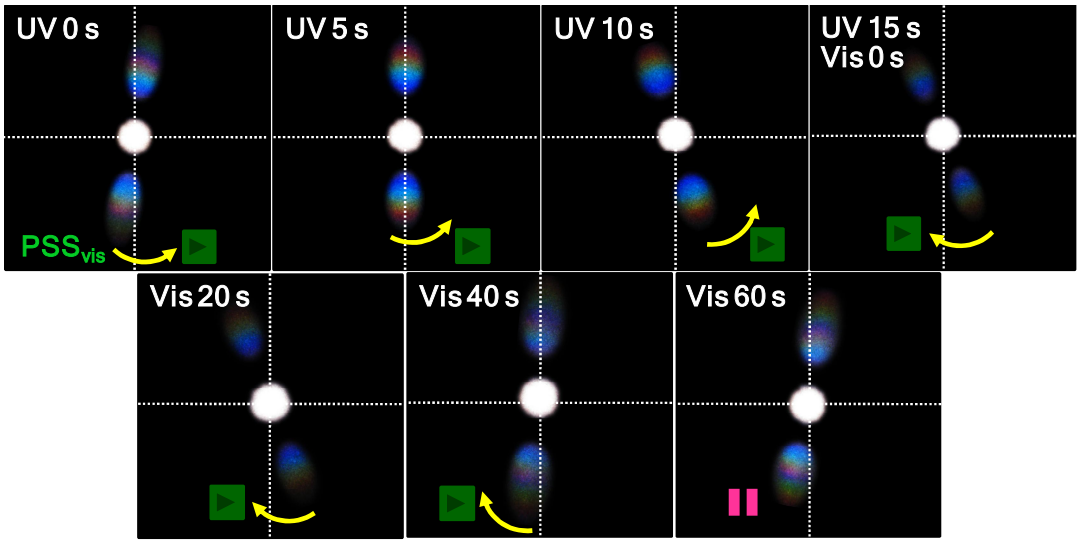

Figure 14 | Reversibility of 2D beam steering driven by the UV and visible light consecutively.

12. Structure of the bilayer LC cell

As depicted in Figure 15, two optically transparent flexible polymethyl methacrylate (PMMA) sheets were used as the substrates, and a third PMMA sheet was inserted between the former two, forming a bilayer LC

cell. The surfaces of the substrates were first coated with an anti-reflection layer and then a polyvinyl alcohol (PVA) film. Such coatings were applied to the inside of the top and the bottom substrates and on both sides of the inserted middle substrate. The alignment direction at the upper part was crossed with that at lower part. The thickness of the top and bottom substrates was 500 μm, while the inserted substrate was 40 μm to minimize the lateral displacement of light.

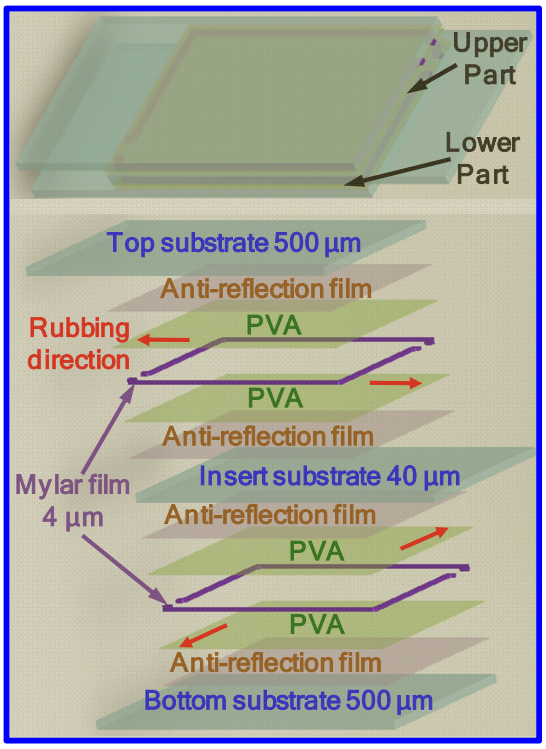

Figure 15 | Schematic illustration of the bilayer LC cell architexture.

References

1. Li, Y., Xue, C., Wang, M., Urbas, A., Li, Q. Photodynamic chiral molecular switches with thermal stability: From reflection wavelength tuning to handedness inversion of self-organized helical superstructures. *Angew. Chem. Int. Ed.* **52**, 13703-13707 (2013).
2. Li, Y., Urbas, A., Li, Q. Reversible light-directed red, green, and blue reflection with thermal stability enabled by a self-organized helical superstructure. *J. Am. Chem. Soc.* **134**, 9573-9576 (2012).
3. Ma, J., Li, Y., White, T., Urbas, A., Li, Q. Light-driven nanoscale chiral molecular switch: reversible

dynamic full range color phototuning. *Chem. Commun.* **45**, 3463-3465 (2010).

4. Yakovlev, D. A., Chigrinov, V. G., Kwok, H. S. *Modeling and Optimization of LCD Optical Performance*. (John Wiley & Sons, New Delhi, 2015).
5. Subacius, D., Bos, P. J., Lavrentovich, O. D. Switchable diffractive cholesteric gratings. *Appl. Phys. Lett.* **71**, 1350-1352 (1997).
6. Subacius, D., Shiyanovskii, S. V., Bos, Ph., Lavrentovich, O. D. Cholesteric gratings with field-controlled period. *Appl. Phys. Lett.* **71**, 3323-3325 (1997).
7. Fuh, A. Y. G., Lin, C. H., Huang, C. Y. Dynamic pattern formation and beam-steering characteristics of cholesteric gratings. *Jpn. J. Appl. Phys.* **41**, 211-218 (2002).
8. Nie, X., Lv, R., Xianyu, H., Wu, T. X., Wu, S. T. Anchoring energy and cell gap effects on liquid crystal response time. *J. Appl. Phys.* **101**, 103110 (2007).